universe

MDPI

*Article*

# Population and Waveform Dependence of Spectral Turnovers in Binary Black-Hole Backgrounds

**Yutong Bai** [1] **and Xiaolong Yang** [2,3,4,*]

[1] Department of Physics, Imperial College London, London SW7 2AZ, UK; yutong.bai24@imperial.ac.uk
[2] Shanghai Astronomical Observatory, Chinese Academy of Sciences, Shanghai 200030, China
[3] Kavli Institute for Astronomy and Astrophysics, Peking University, Beijing 100871, China
[4] Shanghai Key Laboratory of Space Navigation and Positioning Techniques, Shanghai 200030, China
* Correspondence: yangxl@shao.ac.cn

**Abstract**

The spectral turnover of a binary black-hole background depends on both binary formation and coalescence emission. We evaluate a published early two-body primordial-black-hole (PBH) formation rate with mass-dependent pairing and survival suppression, using full inspiral–merger–ringdown (IMR) emission. At a component-mass median of $30M_{\odot}$ and logarithmic width 0.45, replacing a hard innermost-stable-circular-orbit cutoff with IMR emission shifts the peak from 15.3 to 89.2 Hz. A time-only control attributes most of the baseline spectral broadening to redshift weighting, while mass selection changes the peak calibration. We then fit mass, width, and amplitude to test which spectral differences survive parameter adjustment. A phenomenological lognormal template leaves a root-mean-square logarithmic residual of 0.0657 over 10–300 Hz; the residual changes with the target width and frequency band. Within the same early formation channel, two mass mixtures leave residuals of 0.0190 and 0.0765 after a single lognormal is freely refitted, substantially below their moment-matched differences. A general weighted-response representation identifies the source-property combinations probed by these comparisons. All five tested initial mass distributions satisfy the extended-mass OGLE limit over $f_{\rm PBH} = 3 \times 10^{-4}$–$3 \times 10^{-3}$ under the adopted halo and zero-PBH-lens assumptions. The results quantify turnover calibration and spectral approximation errors after refitting a simpler population description.

**Keywords:** gravitational-wave backgrounds; primordial black holes; binary black holes; extended mass distributions; spectral turnovers; population modelling

Check for updates

Academic Editors: Paola Marziani and Gonzalo J. Olmo

Received: 31 July 2026
Revised: 4 November 2026
Accepted: 8 November 2026
Published: 14 November 2026

**Copyright:** © 2026 by the authors. Licensee MDPI, Basel, Switzerland. This article is an open access article distributed under the terms and conditions of the Creative Commons Attribution (CC BY) license.

## 1. Introduction

Binary black-hole backgrounds encode the masses, formation history, and emission of their sources. At nanohertz frequencies, pulsar timing arrays (PTAs) have reported evidence for the spatial correlations expected from gravitational waves (GWs) [1–3]; interpreting that signal requires a population model for supermassive black-hole binaries (SMBHBs) [4]. Here, we study the distinct stellar-mass regime, where the spectral turnover samples inspiral, merger, and ringdown. The central question is how reliably that turnover can be mapped to the initial mass distribution once formation selects which binaries merge.

Primordial black holes (PBHs) are one possible origin of stellar-mass binaries, subject to formation and abundance constraints [5–7]. Their pairing probability and merger rate depend on early binary formation, subsequent perturbations and suppression, and late formation in bound structures [8]. Following early PBH interpretations of resolved mergers [9], calculations have examined tidal torques, binary disruption, perturbed survivors,

and dynamical three-body formation [10–13]. These processes determine both the rate evolution and the mass correlations. Connecting a phenomenological mass distribution to a primordial population therefore requires a formation prescription. The supermassive-PBH interpretation of a PTA signal raises a separate set of abundance, clustering, and formation constraints [14] from those relevant to stellar-mass binaries at higher frequencies.

Stellar-origin binaries also produce a high-frequency background [15], and redshift-dependent mixtures have been studied as a way of separating stellar and primordial populations [16]. The dependence of background predictions on population, rate evolution, and waveform assumptions motivates treating these ingredients together [17]. A turnover can encode a redshifted mass scale, but the mapping from a measured feature to that scale depends on the spectrum emitted by individual binaries and on which binaries actually merge.

We test that mapping through formation-based spectral calculations and refitting experiments. A published early two-body PBH channel supplies the differential merger rate and suppression, and full inspiral–merger–ringdown (IMR) waveforms supply the emitted spectrum. A crossed comparison with the phenomenological rate and hard-ISCO emission establishes the calibration changes; a time-only control separates mass selection from redshift weighting. We then ask which differences remain when mass, width, and amplitude are fitted, rather than fixed. The tests cover two initial mass mixtures, a target-width and abundance grid, and three frequency bands. This complements population-uncertainty studies by quantifying how a specific formation prescription and nonlognormal initial distributions can be absorbed by a refitted lognormal template. The general response representation organizes the calculation, with the inverse-mass scaling used as a consistency relation. Finally, a conditional microlensing calculation checks the adopted abundance against a published numerical limit.

## 2. Population and Emission Model

### *2.1. Distributions, Pairing, and Rate Conventions*

Let $m_1, m_2$ be source-frame component masses, $M_{\rm tot} = m_1 + m_2$ the total mass, $q = \min(m_1, m_2)/\max(m_1, m_2)$ the mass ratio, and

$$\mathcal{M} = \frac{(m_1 m_2)^{3/5}}{M_{\rm tot}^{1/5}} \tag{1}$$

the chirp mass. We reserve $M_c$ for the median of the component-mass distribution and use $M_\odot$ for the solar mass. The number-weighted lognormal probability density, defined with respect to $dm$, is

$$p(m; M_c, \sigma_{\ln}) = \frac{1}{\sqrt{2\pi}\sigma_{\ln} m} \exp\left[-\frac{\ln^2(m/M_c)}{2\sigma_{\ln}^2}\right], \qquad \int_0^\infty p(m)\, dm = 1. \tag{2}$$

Here, $\sigma_{\ln}$ is the standard deviation of $\ln(m/M_c)$, and $\langle m \rangle = M_c \exp(\sigma_{\ln}^2/2)$. In the formation calculation below, $p$ describes the initial PBH population. In the phenomenological control, the same functional form is assigned directly to merging component masses. This distinction allows us to test the mass selection introduced by binary formation.

For the phenomenological control, the differential merger-rate density per unit comoving volume, source proper time, and $dm_1 dm_2$ is

$$R(z; m_1, m_2) = R_{\rm eff,0}\, r(z)\, \pi(m_1, m_2), \qquad r(z) = (1+z)^\alpha \exp[-(z/z_c)^\beta], \tag{3}$$

with $\int \pi \, dm_1 dm_2 = 1$. We integrate labelled components over the full positive quadrant, so no additional factor of two is inserted. The independent prescription is $\pi = p(m_1)p(m_2)$. The equal-mass prescription is instead the singular joint distribution $p(m_1)\delta(m_2 - m_1)$, where $\delta$ is the Dirac delta. These prescriptions have the same one-component marginal but different correlations.

The numerical control fixes $\alpha = 1$, $\beta = 2$, $z_c = 8$, and independent pairing. Its local rate is a reference scale,

$$R_{\mathrm{eff},0} = 1\ \mathrm{Gpc}^{-3}\,\mathrm{yr}^{-1}, \tag{4}$$

with no assumed conversion to PBH abundance. The equal-mass prescription is retained only for the analytical comparisons in Section 3.

### 2.2. An Early Two-Body PBH Formation Benchmark

We implement the unclustered early two-body channel reviewed by Raidal et al. [8], using its differential rate, mass weights, and suppression prescription. This channel describes PBH pairs formed in the early Universe whose coalescence times depend on gravitational torques and whose survival is affected by surrounding objects. We choose a low abundance, $f_{\mathrm{PBH}} = 10^{-3}$, and a fixed matter-perturbation parameter $\sigma_M = 0.005$. Section 4.5 varies both formation inputs around this baseline.

Define the normalized mass-fraction density per unit mass,

$$\phi(m) = \frac{m p(m)}{\langle m \rangle}, \qquad \int \phi(m)\, dm = 1, \qquad \frac{\langle m^2 \rangle}{\langle m \rangle^2} = e^{\sigma_{\ln}^2}, \tag{5}$$

where the moments are number weighted. The mass fraction per logarithmic interval used in Ref. [8] is $m\phi(m)$. With $\eta = m_1 m_2 / M_{\mathrm{tot}}^2$, the rate per $dm_1 dm_2$ is

$$\begin{aligned} \mathcal{R}_{\mathrm{E2}}(z; m_1, m_2) = \mathcal{A} f_{\mathrm{PBH}}^{53/37} \eta^{-34/37} \left(\frac{M_{\mathrm{tot}}}{M_\odot}\right)^{-32/37} \left(\frac{t(z)}{t_0}\right)^{-34/37} \\ \times \phi(m_1)\phi(m_2) S_E(M_{\mathrm{tot}}) S_L(z), \qquad \mathcal{A} = 1.6 \times 10^6\ \mathrm{Gpc}^{-3}\,\mathrm{yr}^{-1}. \end{aligned} \tag{6}$$

Here, $t_0 = t(0)$. We use the full labelled-mass quadrant with the published normalization, without adding a further pair-counting factor. The factors in Equation (6) jointly reweight the initial pairs to determine the merging mass distribution.

For reproducibility, the adopted interpolation for early suppression is

$$\begin{aligned} S_E &= B \left[\frac{e^{\sigma_{\ln}^2}}{\bar{N} + C_0} + \frac{\sigma_M^2}{f_{\mathrm{PBH}}^2}\right]^{-21/74} e^{-\bar{N}}, \qquad B = \frac{\sqrt{\pi}(5/6)^{21/74}}{\Gamma(29/37)}, \\ \bar{N} &= \frac{M_{\mathrm{tot}}}{\langle m \rangle} \frac{f_{\mathrm{PBH}}}{f_{\mathrm{PBH}} + \sigma_M}, \\ C_0 &= \frac{f_{\mathrm{PBH}}^2 e^{\sigma_{\ln}^2}}{\sigma_M^2} \left\{ \left[\frac{\Gamma(29/37)}{\sqrt{\pi}} U\left(\frac{21}{74}, \frac{1}{2}, \frac{5 f_{\mathrm{PBH}}^2}{6\sigma_M^2}\right)\right]^{-74/21} - 1 \right\}^{-1}, \end{aligned} \tag{7}$$

where $U$ is the confluent hypergeometric function of the second kind. These are Equations (46) and (47) of Ref. [8]. We also include its late survival prescription,

$$S_L(z) = \min\left[1,\ 0.01 \tilde{f}^{-0.65} \exp(0.03 \ln^2 \tilde{f})\right], \qquad \tilde{f} = f_{\mathrm{PBH}} \left[\frac{t(z)}{t_0}\right]^{0.44}. \tag{8}$$

At the abundances considered here, $10^{-5} \leq f_{\mathrm{PBH}} \leq 3 \times 10^{-3}$, this prescription gives $S_L = 1$; the nontrivial suppression is $S_E$.

We benchmark Equation (7) against direct integration of the torque-suppression expression in Equation (37) of Ref. [11], with the number-weighted convention in Equation (5). The largest relative difference is 0.86% over $\sigma_{\ln} = 0.2, 0.45, 0.8$ and $M_{\rm tot}/\langle m\rangle = 1, 2, 4, 8$ at the baseline abundance. The adopted channel has separable mass and time factors in this regime, with their functional form fixed by the published formation calculation. For the non-single-lognormal distributions in Section 4.8, we evaluate the direct torque integral with the complete number distribution. The mass-fraction conversion and rate in Equations (5) and (6) apply to any normalized $p(m)$ with the required finite moments; $\langle m^2\rangle/\langle m\rangle^2 = e^{\sigma_{\ln}^2}$ is specific to a single lognormal.

### 2.3. Emission Models and Cosmological Integration

Let $f$ be observed frequency and $f_s = (1+z)f$ source-frame frequency. Our analytical control is the Newtonian, circular, nonspinning inspiral spectrum with a Schwarzschild ISCO cutoff,

$$\frac{dE_{\rm GW}^{\rm ISCO}}{df_s} = \frac{(\pi G)^{2/3}}{3}\mathcal{M}^{5/3} f_s^{-1/3}\Theta\left(\frac{K}{M_{\rm tot}} - f_s\right), \qquad K = \frac{c^3}{6^{3/2}\pi G}, \tag{9}$$

where $G$ is Newton's constant, $c$ the speed of light, and $\Theta$ the step function. With consistent mass units, $K/M_\odot = 4397.17$ Hz. This abrupt termination is compared directly with full coalescence emission.

Phenomenological IMR models incorporate the inspiral, merger, and ringdown [18]. We use the nonspinning limit of IMRPhenomD [19], as implemented in LALSimulation, retaining its dominant quadrupole mode through all three phases. For its face-on Fourier-domain plus polarization at distance $D$, the angle-integrated energy spectrum is

$$\frac{dE_{\rm GW}^{\rm IMR}}{df_s} = \frac{8\pi^2 c^3 D^2}{5G} f_s^2 |\widetilde{h}_{+,\text{face-on}}(f_s)|^2 = \left(\frac{dE}{df_s}\right)_{\rm Newt} T(u,q), \qquad u = \frac{GM_{\rm tot} f_s}{c^3}. \tag{10}$$

The factor $1/5$ follows from integrating the dominant-mode angular pattern; $D$ cancels the waveform's inverse-distance dependence. The Newtonian spectrum in the last expression has no cutoff. We verify $T \to 1$ at low frequency. The frequency-dependent response retains the amplitude evolution through coalescence.

We assess this choice using the updated dominant-mode IMRPhenomXAS model [20] and IMRPhenomXHM [21], which also includes $(\ell, |m|) = (2,1), (3,3), (3,2), (4,4)$ in addition to $(2,2)$. For the spherical-harmonic strain modes, the angle-integrated energy can be written, in the positive-frequency convention used by LALSimulation, as

$$\begin{aligned} \frac{dE_{\rm GW}^{\rm XHM}}{df_s} &= \frac{\pi c^3 D^2}{2G} f_s^2 \sum_{(\ell,m)\in\mathcal{H}_-} |\widetilde{h}_{\ell m}(f_s)|^2, \\ \mathcal{H}_- &= \{(2,-2), (2,-1), (3,-3), (3,-2), (4,-4)\}. \end{aligned} \tag{11}$$

Orthogonality removes interference between distinct modes after angular integration. The negative-$m$ list represents the positive-frequency support in this convention; adding the mirror modes again would count their contribution double. We check this normalization against direct angular integration of the two polarizations. The XAS comparison tests a revised dominant-mode model, while XHM isolates the effect of its additional modes. Equal aligned component spins $\chi_1 = \chi_2 = \pm 0.2$ provide two additional sensitivity tests.

For both emission choices, numerical population comparisons use $q \geq 1/18$, the mass-ratio extent of the IMRPhenomD calibration [19]. Restricting both models to the same domain isolates emission differences. At the baseline width, the excluded early-channel fraction is $8.03 \times 10^{-6}$ of the rate and $5.67 \times 10^{-6}$ of its uncut inspiral energy weight.

At $\sigma_{\ln} = 0.8$, these fractions reach 1.48% and 0.87%, respectively. Section 4.5 tests the corresponding frequency-dependent spectral change directly. The crossed comparison uses zero spins; the additional mode and aligned-spin tests are reported in Section 4.5. A separate XHM calculation extends the domain to $q \geq 10^{-3}$ as a sensitivity test for the omitted pairs, extrapolating the waveform beyond the common calibration domain. The emission calculation is quasi-circular and nonprecessing. Early PBH binaries are born eccentric; this approximation applies to their late coalescence emission [22,23].

Using energy density throughout, define

$$\rho_{c,E} = \frac{3H_0^2c^2}{8\pi G}, \qquad \Omega_{\rm GW}(f) = \frac{1}{\rho_{c,E}}\frac{d\rho_{{\rm GW},E}}{d\ln f}. \tag{12}$$

The population integral is [24]

$$\Omega_{\rm GW}(f) = \frac{f}{\rho_{c,E}H_0}\int_0^{z_{\rm max}}\frac{dz}{(1+z)E(z)}\int dm_1 dm_2\, R(z;m_1,m_2)\,\frac{dE_{\rm GW}}{df_s}\bigg|_{f_s=(1+z)f}. \tag{13}$$

Here, $R$ is given by either Equation (3) or Equation (6). We take $H_0 = 67.4\,{\rm km\,s^{-1}\,Mpc^{-1}}$ and $\Omega_m = 0.315$ [25], with $\Omega_r = 9.2\times10^{-5}$ and $\Omega_\Lambda = 1-\Omega_m-\Omega_r$. Thus,

$$E^2(z) = \Omega_r(1+z)^4 + \Omega_m(1+z)^3 + \Omega_\Lambda, \qquad t(z) = \int_z^\infty \frac{dz'}{(1+z')H_0E(z')}. \tag{14}$$

The benchmark uses $z_{\rm max} = 1000$, with cutoff sensitivity assessed separately. The factor $[(1+z)H(z)]^{-1}$ in Equation (13) converts redshift to source proper time. Rates are per comoving volume and source time; no second time-dilation factor is applied. We discuss the spectrum near its ground-based-frequency turnover, where coalescence emission can be related to the merger rate. The results are ensemble energy densities before detector selection or source subtraction.

## 3. General Spectral Representation and Analytical Controls

### *3.1. Joint Populations and the Weighted Source Response*

Equation (13) extends directly to a joint rate $\mathcal{R}(z,\theta)$, where $\theta = (m_1, m_2, \vec{\chi})$ includes dimensionless intrinsic parameters such as the component spins. For a fixed quasi-circular vacuum emission model, write the source spectrum as the uncut Newtonian spectrum times $T(u,q,\vec{\chi})$. Define the positive measure

$$d\mu = \frac{\mathcal{R}(z,\theta)\mathcal{M}^{5/3}}{(1+z)^{4/3}E(z)}\,dz\,d\theta, \qquad \mathcal{N} = \int d\mu, \qquad 0 < \mathcal{N} < \infty. \tag{15}$$

The integration domain is the chosen population and waveform domain. Substituting the source spectrum gives

$$\Omega_{\rm GW}(f) = C_{\rm GW}f^{2/3}\mathcal{N}\langle T(f\tau,q,\vec{\chi})\rangle_{\mu/\mathcal{N}}, \qquad C_{\rm GW} = \frac{(\pi G)^{2/3}}{3\rho_{c,E}H_0}, \quad \tau = \frac{G(1+z)M_{\rm tot}}{c^3}. \tag{16}$$

Here, $\tau$ has units of time, and brackets denote an average with the normalized measure. This representation allows arbitrary mass–redshift and mass–spin correlations and does not require a lognormal distribution or a factorized merger rate. The numerical examples below specialize it to the early two-body prescription.

Let $\nu$ be the distribution of $(\tau,q,\vec{\chi})$ induced by $d\mu/\mathcal{N}$. Then, the response in Equation (16) is $\int T(f\tau,q,\vec{\chi})\,d\nu$. Two populations with the same $\nu$ have identical spectra up to the constant $\mathcal{N}$ for the same emission model. Equality of $\nu$ is a sufficient condition for this

degeneracy; a finite-band spectrum can also fail to distinguish different $\nu$. This identifies the combination of source parameters that the isotropic spectrum probes and explains why mapping a peak or width to the initial number distribution requires the formation and emission weights.

For physically distinct populations with additive rates, their responses combine with weights $\mathcal{N}_a / \sum_b \mathcal{N}_b$. These weights include chirp mass and redshift. An initial PBH mass mixture within one formation channel is a different construction: Equation (6) includes binaries drawn across its mass components and suppression from the whole distribution. Section 4.8 retains both effects.

### 3.2. Equal-Mass and Independent-Pair Kernels

The following identities apply to Equation (9) with a factorized phenomenological rate. They give closed-form special cases of Equation (16) and independent numerical checks. Write $\Omega(f) = \Omega_{\rm uncut}(f) S(f)$, where the uncut spectrum uses the same population with $\Theta = 1$:

$$W(z) = \frac{r(z)}{(1+z)^{4/3} E(z)}, \qquad I_z = \int_0^{z_{\max}} W(z)\, dz,$$
$$\Omega_{\rm uncut}(f) = \frac{(\pi G)^{2/3} R_{\rm eff,0}}{3 \rho_{c,E} H_0} f^{2/3} I_z \langle \mathcal{M}^{5/3} \rangle. \tag{17}$$

Thus, $S$ is the fraction of the full chirp-mass moment contributed by binaries whose cutoffs exceed $f$, including both their abundance and mass weighting. For equal components, $\mathcal{M}^{5/3} = 2^{-1/3} m^{5/3}$ and the limiting mass is $K/[2(1+z)f]$. Completing the square in the lognormal moment gives

$$S_{\rm eq}(f) = \frac{1}{I_z} \int_0^{z_{\max}} W(z) \Phi\left( \frac{\ln[K/(2M_c f(1+z))] - (5/3)\sigma_{\ln}^2}{\sigma_{\ln}} \right) dz, \tag{18}$$

where $\Phi$ is the standard normal cumulative distribution function. Define $S(f_{1/2}) = 1/2$. At fixed $z_0$, this gives $f_{1/2} = K \exp[-5\sigma_{\ln}^2/3]/[2(1+z_0)M_c]$; the full redshift convolution need not admit a width-independent effective redshift. This half-suppression frequency is distinct from the maximum of $\Omega$, which obeys $d \ln S / d \ln f = -2/3$.

For independent lognormal component masses, introduce

$$x = \frac{\ln(m_1/M_c) + \ln(m_2/M_c)}{2}, \qquad y = \frac{\ln(m_1/M_c) - \ln(m_2/M_c)}{2}, \qquad v = \frac{\sigma_{\ln}^2}{2}. \tag{19}$$

The variables $x, y$ are independent zero-mean normals of variance $v$, with $M_{\rm tot} = 2M_c e^x \cosh y$ and $\mathcal{M}^{5/3} = M_c^{5/3} e^{5x/3} (2\cosh y)^{-1/3}$. Let $g_v$ be that normal density, $a = 5/3$, and $J_v = \int g_v(y) (2\cosh y)^{-1/3} dy$. Then, $\langle \mathcal{M}^{5/3} \rangle = M_c^{5/3} e^{a^2 v/2} J_v$, and analytical integration over $x$ yields

$$S_{\rm ind}(f) = \frac{1}{I_z J_v} \int_0^{z_{\max}} dz\, W(z) \int_{-\infty}^{\infty} dy\, \frac{g_v(y)}{(2\cosh y)^{1/3}} \times \Phi\left( \frac{\ln[K/(2M_c f(1+z)\cosh y)] - av}{\sqrt{v}} \right). \tag{20}$$

This reduces the original mass–redshift integral to a smooth two-dimensional quadrature. The variance $v$ and the $\cosh y$ weights distinguish independent pairing from the equal-mass control.

*3.3. Similarity and the Cutoff-Width Interpretation*

If $m_i = M_c u_i$ and the dimensionless pairing and redshift distributions are independent of $M_c$, the cutoff depends on $f M_c(1+z)(u_1+u_2)$, while the common chirp-mass factor cancels in $S$. Hence,

$$S(f; M_c) = \mathcal{S}(f M_c), \qquad f_{1/2} \propto M_c^{-1}. \tag{21}$$

A mass-dependent rate amplitude also cancels; a changing dimensionless rate shape, a fixed physical mass boundary, or another dimensional emission scale need not. The relation is a similarity check, while its mass calibration concerns the weighted distribution of redshifted total masses.

Let $\ell = \ln(f/\mathrm{Hz})$ and $L = \ln(f_{\rm cut}/\mathrm{Hz})$, where $f_{\rm cut} = K/[(1+z)M_{\rm tot}]$ is drawn with normalized weight proportional to $W(z)\pi(m_1, m_2)\mathcal{M}^{5/3}$. Then,

$$S(f) = \Pr(L > \ell), \qquad P_L(\ell) = -\frac{dS}{d\ell}, \qquad \int P_L(\ell)\, d\ell = 1. \tag{22}$$

Draw $z$ with density $p_z = W/I_z$ and define $Y = \ln(1+z)$, independent of the mass variables under the factorized weight. Exponential tilting shifts the mean of $x$ to $av$ without changing its variance. The logarithmic cutoff variance therefore separates as

$$\begin{aligned} V_L^{\rm eq} &= \sigma_{\ln}^2 + V_Y, \\ V_L^{\rm ind} &= \frac{\sigma_{\ln}^2}{2} + \mathrm{Var}_{\widetilde{g}_v}[\ln(2\cosh y)] + V_Y, \qquad \widetilde{g}_v(y) = \frac{g_v(y)(2\cosh y)^{-1/3}}{J_v}, \end{aligned} \tag{23}$$

with $V_Y = \mathrm{Var}_{p_z}(Y)$. This cutoff-distribution variance is independent of $M_c$ and the rate amplitude and satisfies $V_L \geq V_Y$ for this factorized control. Under the general measure in Equation (15), set $X_M = \ln(M_{\rm tot}/M_\odot)$ and $Y = \ln(1+z)$. The corresponding identity is

$$V_L = \mathrm{Var}_{\mu/\mathcal{N}}(X_M) + \mathrm{Var}_{\mu/\mathcal{N}}(Y) + 2\,\mathrm{Cov}_{\mu/\mathcal{N}}(X_M, Y). \tag{24}$$

Mass–redshift correlations therefore enter the cutoff width explicitly; the lower bound above relies on the independence of the control. For IMR spectra, Section 4.4 instead defines the width of the energy-density peak directly from $\Omega(f)$.

## 4. Formation and Waveform Comparisons

*4.1. Calculation Design and Accuracy*

The fiducial inputs are $M_c = 30M_\odot$, $\sigma_{\ln} = 0.45$, $f_{\rm PBH} = 10^{-3}$, and $\sigma_M = 0.005$. We compute the two population prescriptions with both emission models, producing four spectra. For shape comparisons, each retained population is divided by its own local merger rate and rescaled to 1 $\mathrm{Gpc}^{-3}\,\mathrm{yr}^{-1}$. This common normalization isolates population and emission effects; the physical rate predicted by Equation (6) is reported separately.

We integrate in $x$, $|y|$, and $\ln(1+z)$, using the variables of Equation (19). Uniform logarithmic grids permit convolution of the common mass scale with redshift, while the Gauss–Legendre quadrature rule treats the mass ratio. The baseline logarithmic spacing is at most 0.005, with 48 mass-ratio nodes and 601 output frequencies from 0.02 to $2 \times 10^4$ Hz. The broad frequency grid brackets the spectral features; figures focus on the turnover band. Halving the spacing, doubling the mass-ratio nodes, and using 1201 output frequencies changes $\Omega$ by at most 0.21% where it exceeds $10^{-3}$ of its peak, over $\sigma_{\ln} = 0.2, 0.45, 0.8$ and all four combinations. Changes in peak frequency and logarithmic half-maximum width are below 0.005% and 0.0005%, respectively. Independent local-rate, monochromatic-limit, suppression, and waveform checks are described in Appendix A. Additional XAS/XHM refinements, including the spin tests, change spectra by less than 0.08% over the same

relative-amplitude domain. Direct three-variable quadrature without convolution reproduces the fiducial IMR spectrum at 10, 25, 100, and 300 Hz to better than 0.008%.

### *4.2. Formation-Selected Masses and the Local Rate*

Figure 1 shows how the early two-body prescription changes both amplitude and mass weighting. The suppressed rate follows from the specified abundance and initial mass distribution. For the fiducial inputs, the full local rate is 2.93052 $\mathrm{Gpc}^{-3}\,\mathrm{yr}^{-1}$, and the retained $q \geq 1/18$ rate is 2.93050 $\mathrm{Gpc}^{-3}\,\mathrm{yr}^{-1}$. Removing $S_E$ changes the abundance–rate relation even though $S_L = 1$ throughout this scan.

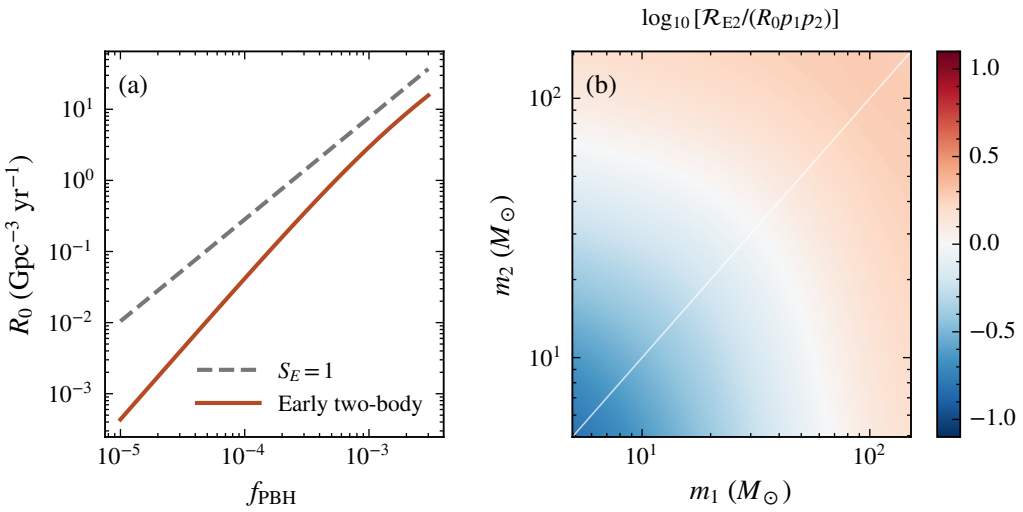



**Figure 1.** Formation-based rate benchmark for $M_c = 30M_\odot$, $\sigma_{\ln} = 0.45$, and $\sigma_M = 0.005$. (**a**) Local rate integrated over $q \geq 1/18$, as a function of PBH abundance, with early suppression (solid) and with $S_E$ set to unity (dashed); $S_L = 1$ throughout. (**b**) Differential rate at $z = 0$, divided by $R_0 p(m_1) p(m_2)$, at $f_{\mathrm{PBH}} = 10^{-3}$. Here, $R_0$ is the full-quadrant early-channel rate, so the map displays the departure of the normalized merging distribution from independent draws of the initial number distribution. The diagonal is $m_1 = m_2$. The map concerns the rate prescription; the waveform calculations separately restrict $q \geq 1/18$.

The ratio in panel (b) is not constant: total mass, symmetric mass ratio, conversion to mass fractions, and survival probability reweight the initial pairs. This distinction also appears in a time-only control. That control retains $p(m_1)p(m_2)$ and replaces $r(z)$ by $[t(z)/t_0]^{-34/37} S_L(z)/S_L(0)$, while fixing the same local normalization. With IMR emission, changing the time dependence alone moves the peak from 106.95 to 96.21 Hz and increases $\mathcal{W}$ from 2.2246 to 2.9419. Adding the early-channel mass weights then moves the peak to 89.21 Hz, a further 7.28% decrease, while changing the width to 2.9414 (−0.017%). The baseline broadening is therefore dominated by the time dependence; the mass weights chiefly change the peak calibration in this comparison.

### *4.3. Replacing the Source Spectrum*

Figure 2 compares the source responses. IMR emission extends beyond the ISCO frequency and develops merger structure that depends on mass ratio. In particular, the equal-mass response $T$ exceeds unity near merger. Consequently, $T$ is not a survival probability for a distribution of termination frequencies. Population averaging can make a particular response smooth and monotone, but it does not restore the general cumulative-distribution identity in Equation (22).

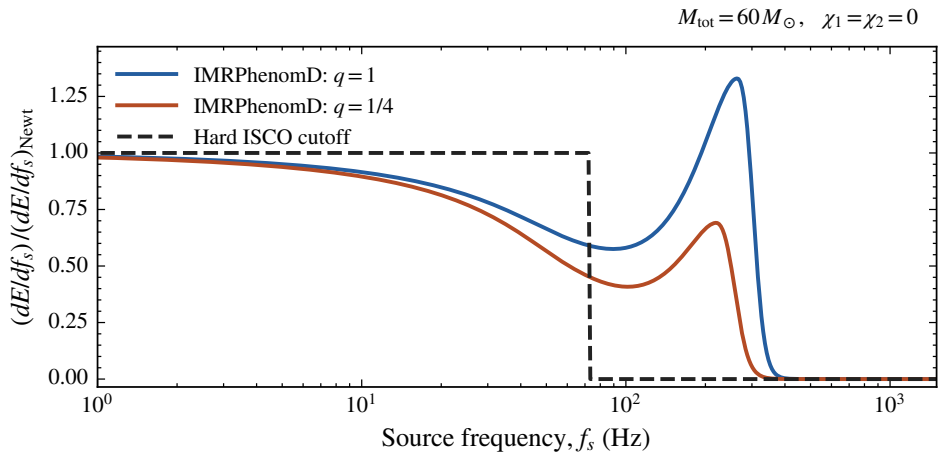



**Figure 2.** Source energy spectrum relative to uncut Newtonian inspiral for a nonspinning binary of total mass $60M_\odot$. IMRPhenomD includes the dominant-mode inspiral, merger, and ringdown for $q = 1$ and $q = 1/4$. The dashed curve is the hard-ISCO control. Frequencies are in the source frame. The low-frequency limit tends to unity; the merger excess and subsequent decay demonstrate why a cutoff probability kernel cannot generally represent this response.

The population-level effect is displayed in Figure 3. For the phenomenological rate, replacing the ISCO model moves the peak from 19.6 to 106.9 Hz, a factor of 5.45. For the early two-body channel, the peak moves from 15.3 to 89.2 Hz, a factor of 5.81. The lower panel shows the frequency-dependent changes, including the loss of high-frequency power caused by the abrupt cutoff.

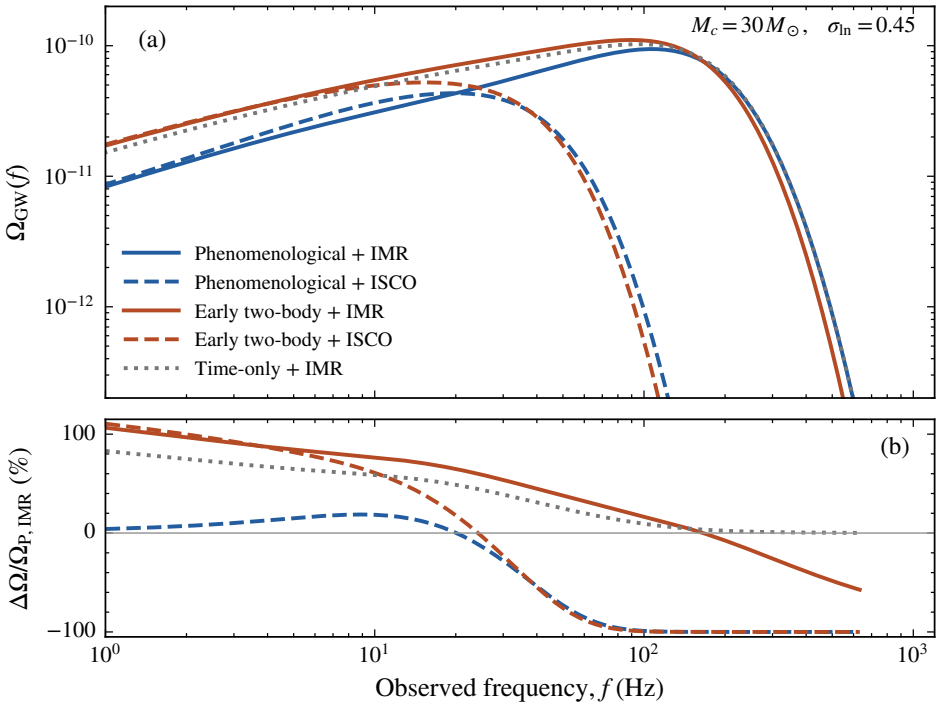



**Figure 3.** Population and emission effects at $M_c = 30M_\odot$ and $\sigma_{\ln} = 0.45$. Every curve has the same retained local rate, 1 $\mathrm{Gpc^{-3}\,yr^{-1}}$, and uses $q \geq 1/18$. Colour identifies the phenomenological or early two-body population; solid and dashed lines identify IMRPhenomD and hard-ISCO emission. The dotted time-only control isolates the redshift-history change. (**a**) Ensemble energy-density spectra. (**b**) Relative difference from the phenomenological IMR spectrum, $100(\Omega - \Omega_{\rm P,IMR})/\Omega_{\rm P,IMR}$. Ratios are displayed only where the reference exceeds $10^{-3}$ of its peak. All parameters are prescribed for this model comparison.

### *4.4. Peak, Width, and Conditional Mass Calibration*

For both source models, define descriptors directly from the calculated energy density:

$$f_{\rm peak} = \arg\max_f \Omega_{\rm GW}(f), \qquad \Omega_{\rm GW}(f_-) = \Omega_{\rm GW}(f_+) = \frac{1}{2}\Omega_{\rm GW}(f_{\rm peak}), \qquad \mathcal{W} = \ln\left(\frac{f_+}{f_-}\right), \tag{25}$$

where $f_- < f_{\rm peak} < f_+$ represents the crossings around the single peak found in these calculations. The logarithmic full width at half maximum $\mathcal{W}$ describes the energy-density peak; it differs from the cutoff variance $V_L$ and the half-suppression frequency $f_{1/2}$ in Section 3.

Table 1 separates the two effects quantitatively. With IMR held fixed, the early-channel peak is 16.6% lower than the phenomenological peak and its width is 32.2% larger. The time-only ablation in Section 4.2 attributes almost all of this baseline broadening to redshift weighting. Figure 4 extends the comparison over $\sigma_{\ln} \in \{0.2, 0.3, 0.45, 0.6, 0.8\}$. Broader initial distributions lower the peak and generally broaden it, while the amount and even the sign of the width change between ISCO and IMR depend on the population and initial width. A single additive waveform correction to a cutoff-width formula is therefore inadequate over this scan.

**Table 1.** Spectral descriptors at $M_c = 30M_\odot$ and $\sigma_{\ln} = 0.45$. Amplitudes use the common retained local rate of 1 Gpc$^{-3}$ yr$^{-1}$. The last two rows isolate the redshift-history contribution by retaining independent initial-number pairing.

| Population | Emission | $f_{\rm peak}$ (Hz) | $f_-$ (Hz) | $f_+$ (Hz) | $\mathcal{W}$ |
|---|---|---|---|---|---|
| Phenomenological | ISCO | 19.61 | 3.97 | 47.36 | 2.478 |
| Phenomenological | IMR | 106.95 | 23.73 | 219.52 | 2.225 |
| Early two-body | ISCO | 15.34 | 2.08 | 41.80 | 3.000 |
| Early two-body | IMR | 89.21 | 10.37 | 196.39 | 2.941 |
| Time-only control | ISCO | 16.56 | 2.24 | 45.29 | 3.005 |
| Time-only control | IMR | 96.21 | 11.25 | 213.11 | 2.942 |

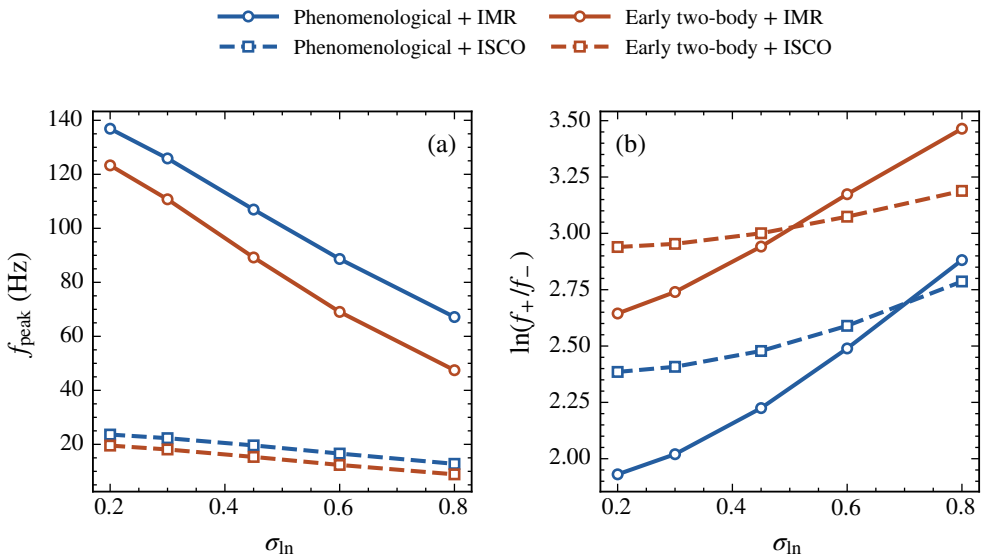



**Figure 4.** Dependence of the spectral peak (**a**) and logarithmic full width at half maximum (**b**) on the initial lognormal width, at $M_c = 30M_\odot$. Colours and line styles match Figure 3; markers denote the five calculated widths, with connecting lines as visual guides. The early channel fixes $f_{\rm PBH} = 10^{-3}$ and $\sigma_M = 0.005$. All spectra use $q \geq 1/18$; the excluded rate fraction reaches 1.48% for the broadest early-channel distribution. Numerical convergence errors are smaller than the markers.

The inverse-mass similarity remains a useful check. At fixed dimensionless initial width, abundance, and $\sigma_M$, the early-channel mass kernel rescales homogeneously under $m_i \mapsto \lambda m_i$. In particular, $M_{\rm tot}/\langle m \rangle$, $\eta$, and $S_E$ are invariant, while the local rate acquires a common factor. The nonspinning IMR response depends on $M_{\rm tot} f_s$, so the normalized spectral shape shifts horizontally under the same transformation. We verify $M_c f_{\rm peak} \simeq 2676.23\ M_\odot$ Hz and constant $\mathcal{W}$ at $M_c = 10, 30, 100 M_\odot$ for the early IMR benchmark. This verifies the expected mass similarity of the formation and emission kernels.

The calibration coefficient matters even when the slope is fixed. Take the early-channel IMR spectrum with $M_c = 30 M_\odot$ as a synthetic target and keep $\sigma_{\ln} = 0.45$ fixed. Matching only its peak with the phenomenological IMR model gives $M_c = 35.97 M_\odot$; matching it with the phenomenological ISCO model gives $6.60 M_\odot$. These conditional matches allow a free amplitude while holding the initial width fixed. They illustrate how emission and population choices enter the inferred mass scale. The unequal widths in Table 1 also show why neither match reproduces the whole target spectrum.

### *4.5. Waveform and Formation-Input Sensitivity*

Figure 5 tests the IMR calibration by comparing PhenomD, XAS, and XHM at $\sigma_{\ln} = 0.2, 0.45, 0.8$. At the baseline width, their nonspinning peaks are 89.21, 87.81, and 89.48 Hz, with $\mathcal{W} = 2.9414$, 2.9620, and 2.9223, respectively. Across these three widths, the largest pairwise peak difference among the nonspinning models is 3.6%. This is much smaller than the ISCO–IMR change, while remaining relevant to precise mass calibration. The additional XHM modes move the peak upward relative to XAS; their contribution grows for broader mass distributions.

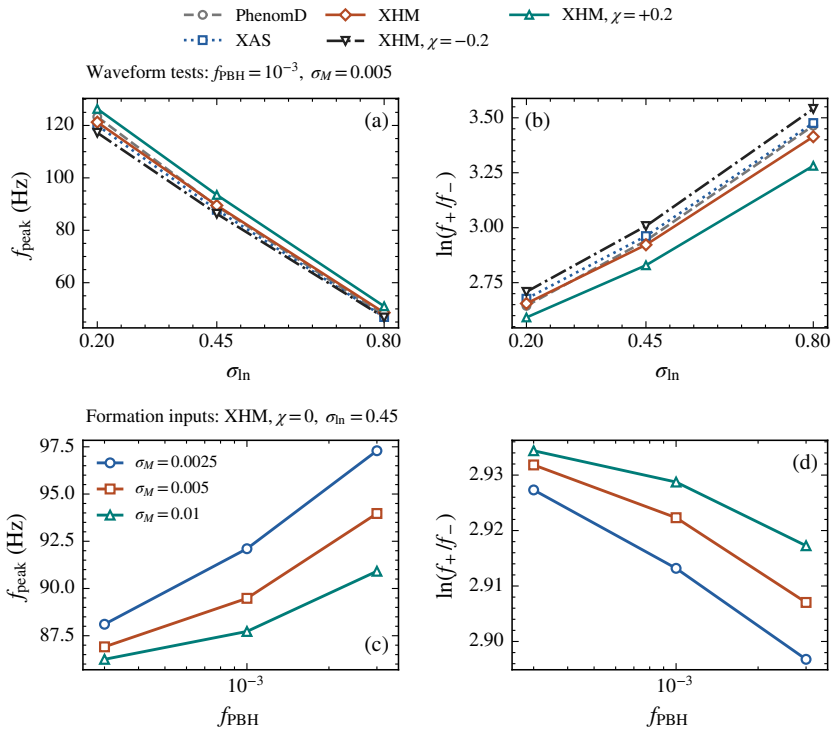



**Figure 5.** Sensitivity of the early-channel spectral peak and logarithmic half-maximum width, at $M_c = 30 M_\odot$ and $q \geq 1/18$. (**a**) Peak frequency and (**b**) logarithmic half-maximum width versus $\sigma_l n$ for three nonspinning IMR prescriptions and two equal aligned-spin XHM tests, at fixed $f_{\rm PBH} = 10^{-3}$ and $\sigma_M = 0.005$. Curves without a spin label have $\chi_1 = \chi_2 = 0$; otherwise, $\chi_1 = \chi_2 = \chi$. (**c**) Peak frequency and (**d**) logarithmic half-maximum width versus $f_{\rm PBH}$ for the three indicated $\sigma_M$ values, using nonspinning XHM and $\sigma_l n$ = 0.45. Markers denote calculations; connecting lines guide the eye. The scans use prescribed parameter values.

Equal aligned spins $\chi_1 = \chi_2 = -0.2$ and $+0.2$ change the baseline XHM peak to 86.30 and 93.50 Hz and the width to 3.0077 and 2.8290. The mass-width trend persists over the tested spin choices, but the calibration depends on spin. Extending the nonspinning XHM integration to $q \geq 10^{-3}$ changes the absolute spectrum by at most 0.285% over 10–300 Hz for the broadest tested width, $\sigma_{\ln} = 0.8$, with a 0.112% peak shift. At the baseline width, the spectral change is below 0.0003%. These frequency-resolved tests supplement the integrated-tail fractions quoted in Section 2.3.

To test the fixed formation inputs, we evaluate the nine combinations $f_{\rm PBH} \in \{3 \times 10^{-4}, 10^{-3}, 3 \times 10^{-3}\}$ and $\sigma_M \in \{0.0025, 0.005, 0.01\}$ with nonspinning XHM at $\sigma_{\ln} = 0.45$. These bracket the baseline by factors of approximately three and two, respectively. The retained local rate spans 0.247–15.68 $\mathrm{Gpc^{-3}\,yr^{-1}}$; the peak spans 86.25–97.29 Hz and $\mathcal{W}$ spans 2.8968–2.9344. Rate normalization is therefore much more sensitive than the normalized shape over this grid. The residual shape dependence arises because $S_E$ depends on $M_{\rm tot}/\langle m \rangle$ and on $f_{\rm PBH}/\sigma_M$, changing the relative weights of merging masses.

### *4.6. Matching Two Descriptors Versus the Full Spectrum*

Differences at fixed $M_c$ and $\sigma_{\ln}$ need not survive parameter adjustment. We use the early-channel nonspinning XHM spectrum at $(M_c, \sigma_{\ln}) = (30M_\odot, 0.45)$ as a synthetic target. In this subsection and the subsequent mixture fits, early suppression is evaluated by the direct torque integral. A phenomenological XHM template with $(M_c/M_\odot, \sigma_{\ln}) = (21.658, 0.84154)$ matches the target's peak and width to better than $10^{-5}$ fractionally before rounding. These two descriptors therefore admit a mass–width degeneracy even between the two specified population prescriptions.

To compare entire spectra, define

$$\epsilon_{\ln\Omega} = \left[\frac{1}{N}\sum_{i=1}^{N} \ln^2\!\left(\frac{A\Omega_{\rm tmp}(f_i)}{\Omega_{\rm tgt}(f_i)}\right)\right]^{1/2}, \tag{26}$$

where $A > 0$ is a free amplitude and each spectrum is normalized to unit retained local rate. We use $N = 301$ equally spaced points in $\ln f$, including both endpoints of the stated band. The optimum $\ln A$ is the mean of $\ln\Omega_{\rm tgt} - \ln\Omega_{\rm tmp}$. This deterministic objective gives equal weight per logarithmic frequency interval. Detector inference would instead weight residuals through the measured covariance and include the other source populations.

On 10–300 Hz, the two-descriptor match leaves $\epsilon_{\ln\Omega} = 0.242$ after fitting $A$, with a maximum fractional residual of 171%. Allowing $M_c$, $\sigma_{\ln}$, and $A$ to vary gives $(M_c/M_\odot, \sigma_{\ln}, A) = (33.480, 0.62278, 1.272)$, $\epsilon_{\ln\Omega} = 0.0657$, and a maximum fractional residual of 17.5%. The search uses $10 \leq M_c/M_\odot \leq 100$ and $0.15 \leq \sigma_{\ln} \leq 1.1$. Figure 6 shows the reduction in distributed spectral error when exact agreement of two summaries is replaced by a full-spectrum fit.

We repeat the free-parameter fit for nine early-channel targets with $M_c = 30M_\odot$, $\sigma_{\ln} \in \{0.2, 0.45, 0.8\}$ and $f_{\rm PBH} \in \{3 \times 10^{-4}, 10^{-3}, 3 \times 10^{-3}\}$, fixing $\sigma_M = 0.005$. Each target is fitted independently on 10–100, 10–300, and 20–500 Hz. Figure 7 displays all 27 residuals. On 10–300 Hz, they span 0.0316–0.0945: broader targets are more closely approximated by a refitted phenomenological template over this grid. For the baseline target, the three bands give $\epsilon_{\ln\Omega} = (0.0163, 0.0657, 0.0584)$, respectively. Two additional baseline-width targets with $\sigma_M = 0.0025$ and 0.01 give a 10–300 Hz range of 0.0655–0.0658 when combined with the central value. The residual size is therefore conditional on both the population inputs and the chosen fitting band.

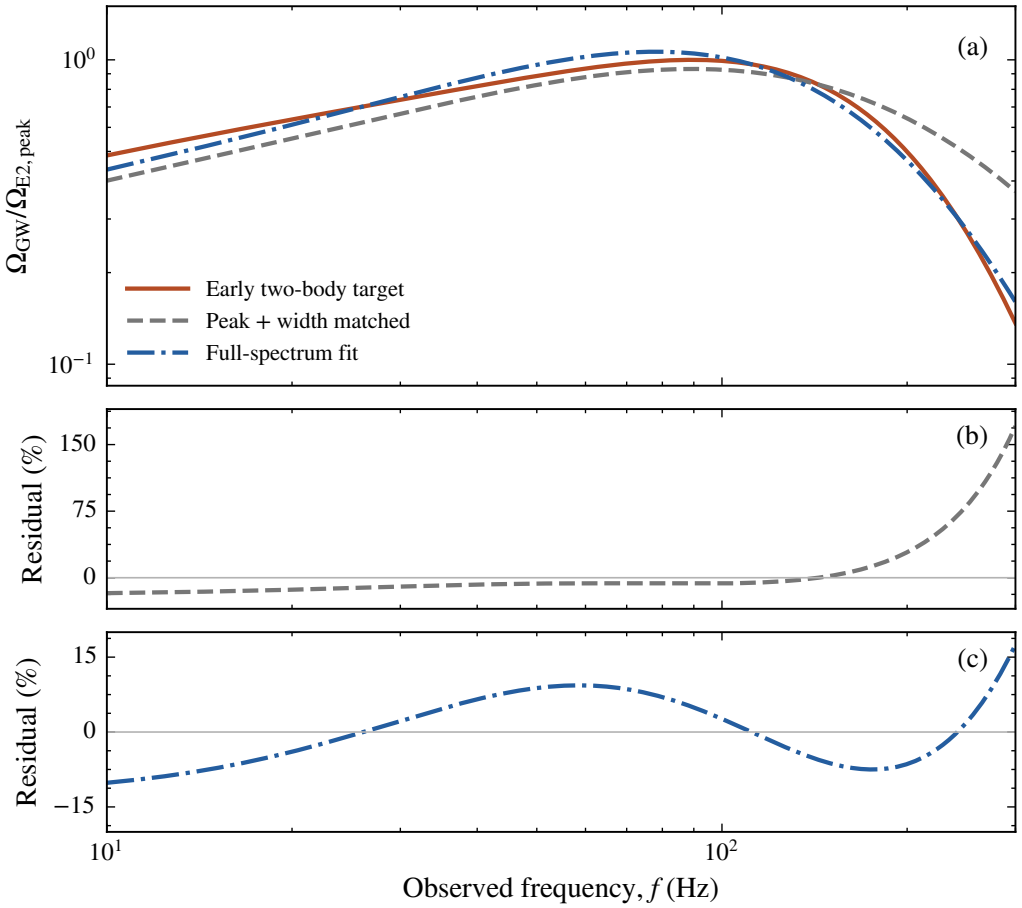



**Figure 6.** Nonspinning XHM fits on 10–300 Hz, using direct suppression for the early-channel target. (**a**) Target at $(M_c/M_\odot, \sigma_{\ln}) = (30, 0.45)$, a phenomenological template matching its peak and width, and a phenomenological full-spectrum fit. Curves are divided by the target's peak; the two template amplitudes separately minimize Equation (26). (**b**) Fractional residual $100(A\Omega_{\rm tmp}/\Omega_{\rm tgt} - 1)$ for the peak-and-width match. (**c**) Fractional residual for the full-spectrum fit. The two residual panels use different vertical scales; the thin grey horizontal lines mark zero residual.

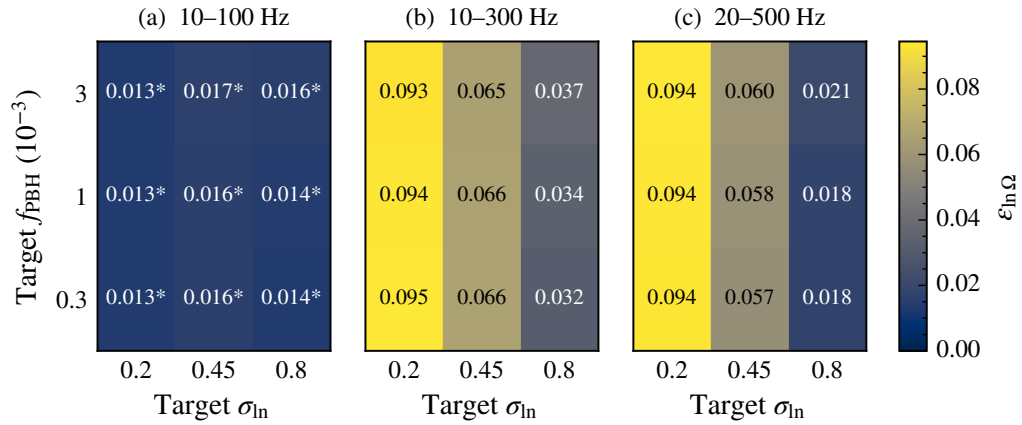



**Figure 7.** Residuals after fitting the phenomenological template's mass, width, and amplitude to nine early-channel XHM targets, with direct suppression, $M_c = 30M_\odot$, and $\sigma_M = 0.005$ for the targets. The fitting bands are (**a**) 10–100 Hz, (**b**) 10–300 Hz, and (**c**) 20–500 Hz; every fit uses 301 equal-log-frequency points. Colours and cell values give $\epsilon_{\ln\Omega}$. An asterisk marks a solution at the stated common mass or width boundary. The text reports a separate expanded-bound check for the short band.

The 10–100 Hz fits reach a mass or width boundary in all nine grid cases. Repeating those short-band comparisons with $1 \leq M_c/M_\odot \leq 150$ and $0.15 \leq \sigma_{\ln} \leq 1.6$ gives seven interior solutions; two still reach the upper width boundary. For the baseline target, the fit moves from $(M_c/M_\odot, \sigma_{\ln}) = (14.31, 1.100)$ to $(3.77, 1.600)$ and reduces the residual from 0.0163 to 0.0105. The short-band fit thus permits substantial parameter shifts with small spectral changes. For independent lognormal components, the excluded pair fraction is $\mathrm{erfc}[\ln 18/(2\sigma_{\ln})]$, where erfc is the complementary error function. It ranges from 6.46% to 20.15% in these expanded fits, so their interpretation is tied to the retained $q \geq 1/18$ template family. Both searches and their boundary flags are supplied; Appendix A separately checks the mass-ratio sensitivity of the three main 10–300 Hz fits.

### *4.7. High-Redshift Sensitivity of the Descriptors*

For the early-channel IMR calculation, varying the integration cutoff from $z_{\max} = 300$ to 1000 and 2000 leaves $f_{\mathrm{peak}} = 89.21$ Hz and $\mathcal{W} = 2.9414$ stable to the displayed precision. By contrast, the last descending crossing of $\Omega/\Omega_{\mathrm{uncut}} = 1/2$ shifts from 19.12 to 16.85 and 16.06 Hz, respectively. The uncut inspiral normalization includes chirp-mass weight from high redshift even when those binaries emit little near the observed turnover. Normalizing by that extrapolation can therefore move $f_{1/2}$ without appreciably moving the spectral peak. This is a further reason to use Equation (25) for the physical comparison.

This cutoff test concerns coalescence emission near the ground-based-frequency turnover. Extending the calculation to the low-frequency background of long-lived binaries requires following their orbital population and emission history.

### *4.8. Beyond a Single Lognormal Mass Distribution*

The rate in Equation (6) also permits an initial distribution with multiple components. Write $\mathcal{L}_{a,b}(m) = p(m; aM_\odot, b)$ and consider two number-weighted mixtures,

$$\begin{aligned} p_A(m) &= 0.8\mathcal{L}_{30,0.45}(m) + 0.2\mathcal{L}_{80,0.25}(m), \\ p_B(m) &= 0.5\mathcal{L}_{20,0.25}(m) + 0.5\mathcal{L}_{60,0.25}(m). \end{aligned} \tag{27}$$

For each mixture, construct a single lognormal with the same first two number-weighted mass moments. Its parameters are

$$\sigma_*^2 = \ln\frac{\langle m^2\rangle}{\langle m\rangle^2}, \qquad M_* = \langle m\rangle e^{-\sigma_*^2/2}. \tag{28}$$

These give $(M_*/M_\odot, \sigma_*) = (36.872, 0.55724)$ for $A$ and $(35.777, 0.53446)$ for $B$. The respective means are 43.065 and $41.270M_\odot$. We retain all cross-component pairs in $\phi(m_1)\phi(m_2)$ and evaluate the direct torque-suppression integral for each complete distribution. Thus, each comparison uses the same formation channel, abundance, and emission prescription while changing higher moments and the shape of the initial mass distribution. Table 2 summarizes the retained local merger rates and spectral descriptors for the baseline distribution, the two mixtures, and their moment-matched lognormal controls.

Both mixtures give a single spectral peak. Relative to their moment-matched controls, their peak frequencies decrease by 3.94% and 2.72%, and their widths by 1.05% and 4.86%. The local rates differ by only 0.18% and 0.40%. Allowing only a constant amplitude on 10–300 Hz leaves $\epsilon_{\ln\Omega} = 0.0530$ for $A$ and 0.1350 for $B$. This moment-matched comparison establishes dependence on the full initial distribution.

A stronger test releases the lognormal median and width as well as its amplitude. Target and template use the same early formation channel, direct torque suppression, nonspinning XHM emission, and prescribed $f_{\mathrm{PBH}}$ and $\sigma_M$. Each spectrum is divided by

its own retained local rate before fitting the free amplitude, so the comparison tests shape without requiring agreement of the predicted rates. Table 3 and Figure 8 give the result: the remaining residuals are 0.0190 and 0.0765, reductions by factors of 2.8 and 1.8 relative to moment matching. The fitted mass distributions need not preserve the target's initial moments. Much of the moment-matched difference can therefore be absorbed by changing the single-lognormal parameters.

**Table 2.** Non-single-lognormal test with nonspinning XHM, $f_{\rm PBH} = 10^{-3}$, $\sigma_M = 0.005$, $z_{\rm max} = 1000$, and $q \geq 1/18$. All rows use direct torque suppression, including the single-lognormal controls. Rates are denoted as retained local rates in $\mathrm{Gpc^{-3}\,yr^{-1}}$. The baseline is $\mathcal{L}_{30,0.45}$; the moment-matched parameters are defined above.

| Initial Number Distribution | $R_0$ | $f_{\rm peak}$ (Hz) | $\mathcal{W}$ |
|---|---|---|---|
| Baseline lognormal | 2.9190 | 89.45 | 2.9223 |
| Mixture $A$ | 2.2735 | 58.77 | 3.0439 |
| Lognormal matched to $A$ | 2.2777 | 61.18 | 3.0762 |
| Mixture $B$ | 2.3666 | 63.73 | 2.8951 |
| Lognormal matched to $B$ | 2.3761 | 65.51 | 3.0429 |

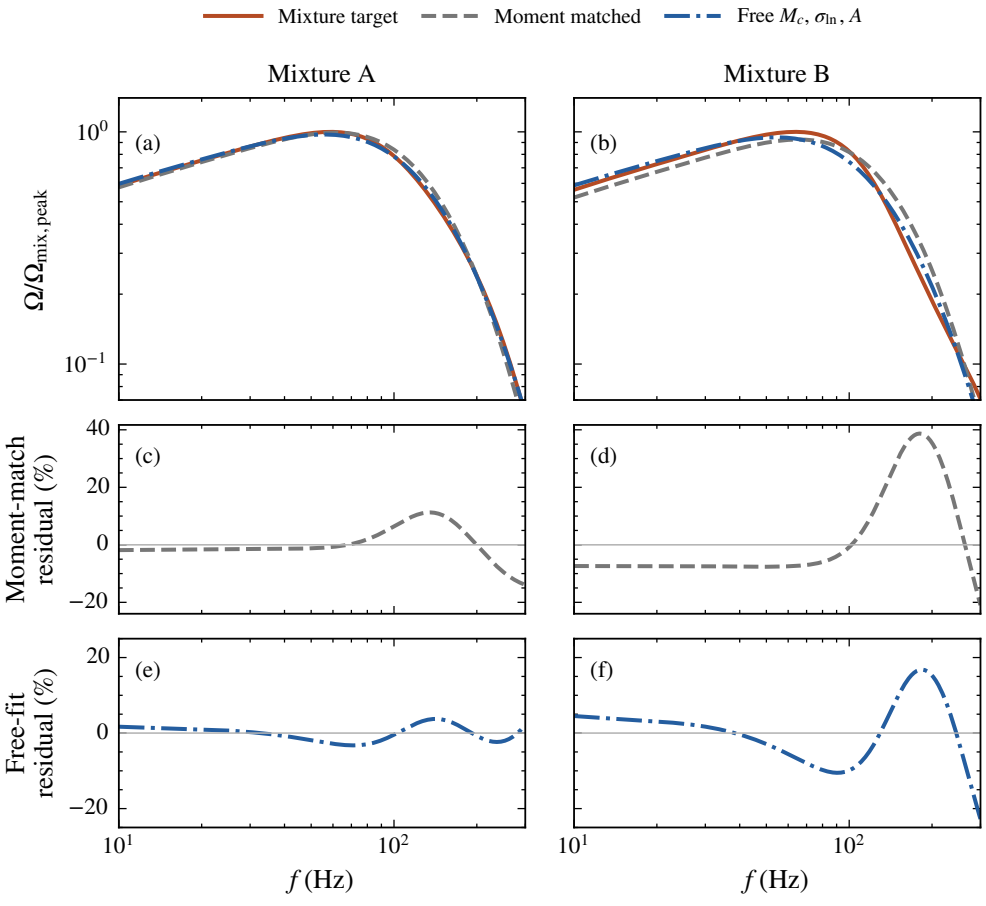



**Figure 8.** Moment matching and free-parameter fitting for mixtures $A$ (**left**) and $B$ (**right**), with the same early formation channel, direct suppression, and nonspinning XHM throughout. (**a**) Target and fitted spectra for mixture A and (**b**) mixture B, normalized to each target's peak. (**c**) Fractional residuals of the moment-matched lognormal for mixture A and (**d**) mixture B, after fitting only its amplitude. (**e**) Residuals after fitting mass, width, and amplitude for mixture A and (**f**) mixture B. The two residual rows use separate vertical scales; both columns share the scale within each row.

Changing the fitting band to 10–100 and 20–500 Hz gives residuals $(0.0022, 0.0395)$ for $A$ and $(0.0029, 0.1013)$ for $B$, respectively. These comparisons keep the formation prescription fixed and test how closely a single lognormal can approximate each mixture's spectrum. The representation in Section 3.1 expresses this agreement through the energy-weighted source response. The free amplitude is a shape-fitting parameter; Section 5.2 checks the prescribed initial abundances separately.

**Table 3.** Free single-lognormal fits to the two mixture spectra on 10–300 Hz. Targets and templates share the early channel and nonspinning XHM emission. The objective and bounds are those of Section 4.6. The amplitude $A$ multiplies a template normalized to unit retained local rate. The last column gives the maximum absolute fractional residual.

| Target | $M_c/M_\odot$ | $\sigma_{\ln}$ | $A$ | $\epsilon_{\ln\Omega}$ | Max. Residual |
|---|---|---|---|---|---|
| Mixture $A$ | 34.911 | 0.64106 | 1.0411 | 0.0190 | 3.75% |
| Mixture $B$ | 35.723 | 0.64541 | 0.9935 | 0.0765 | 22.76% |

## 5. Observational Interpretation and Model Scope

### 5.1. Physical Normalization and LVK Context

Restoring the early-channel rate predicted at the fiducial abundance, the IMR calculation gives

$$R_{0,q\geq 1/18} = 2.9305\ \mathrm{Gpc}^{-3}\,\mathrm{yr}^{-1}, \qquad \Omega_{\mathrm{GW}}(25\ \mathrm{Hz}) = 2.2588\times 10^{-10}. \tag{29}$$

The corresponding amplitude per unit local rate is $7.7079\times 10^{-11}$. This physical normalization follows Equation (6); the spectra in Figure 3 instead use the common rate to isolate shape differences.

For a fixed power-law index $\alpha_{\mathrm{GW}} = 2/3$ and reference frequency 25 Hz, the LIGO–Virgo–KAGRA (LVK) O1–O3 analysis reported $\Omega_{\mathrm{ref}} \leq 3.4\times 10^{-9}$ at 95% credibility with a log-uniform amplitude prior [26]. The original O1–O4a report gave $2.0\times 10^{-9}$ [27]. The update through 1 April 2025 reports $2.0\times 10^{-9}$ and recomputes the earlier O1–O4a result as $2.8\times 10^{-9}$ under revised frequency cuts [28]. Our benchmark amplitude at 25 Hz is about 8.9 times smaller than the updated $2.0\times 10^{-9}$ reference. These power-law limits set the observational amplitude scale; a constraint on the curved benchmark spectrum requires its own spectral template.

A statistical test would weight the full spectral template with the measured cross-correlation spectrum and covariance [29,30]. Resolved events provide additional information: the GWTC-4.0 population analysis reports a local binary black-hole rate of approximately 14–26 $\mathrm{Gpc}^{-3}\,\mathrm{yr}^{-1}$ at central 90% credibility [31]. Assigning part of that rate to the present channel requires its mass distribution, selection effects, and a stellar-origin contribution. Equation (29) supplies the rate and amplitude for that specified benchmark.

### 5.2. Abundance and Complementary Population Information

Because $p(m)$ specifies the initial PBH population in the formation model, its abundance density is $\psi(m) = f_{\mathrm{PBH}}\phi(m)$, with $\int \psi(m)dm = f_{\mathrm{PBH}}$. For a response linear in abundance and an applicable monochromatic constraint $f_{\max}(m)$, the extended-distribution test [32] is

$$\int \frac{\psi(m)}{f_{\max}(m)}\,dm \leq 1. \tag{30}$$

We evaluate this test using the numerical OGLE limits of Mróz et al. [33,34], taking the strict 95% column that assigns the detected events to stellar lenses and hence assumes zero PBH lenses. This column is proportional to $1/N_{\mathrm{exp}}(f_{\mathrm{PBH}} = 1, m)$, so the expected PBH count

adds linearly over mass. We adopt that analysis's contracted Milky Way halo, LMC halo, and velocity model, with PBHs tracing their dark matter and negligible mass evolution between the initial population and the lens population. These assumptions define the conditional abundance check.

Writing $J = \int \phi(m)/f_{\max}(m)\, dm$, the conditional extended-distribution limit is $f_{95}^{\rm ext} = J^{-1}$ and the normalized expected PBH count is $\mathcal{I} = f_{\rm PBH} J$. The authors' table spans $10^{-6}$–$10^{4} M_\odot$. We integrate in $\ln m$, using the mass-weighted density $m^2 p(m)/\langle m \rangle$ and shape-preserving interpolation of $\ln f_{\max}$. Table 4 gives the results for the five tested initial distributions.

**Table 4.** Conditional OGLE abundance check under the zero-PBH-lens and halo assumptions stated in the text. The lognormal rows have $M_c = 30 M_\odot$. The normalized expected count $\mathcal{I}$ is evaluated at the fiducial abundance $10^{-3}$; a value below unity satisfies this test.

| Initial Number Distribution | $f_{95}^{\rm ext}$ | $\mathcal{I}$ | $N_{\rm exp}^{\rm PBH}$ |
|---|---|---|---|
| Lognormal, $\sigma_{\ln} = 0.20$ | 0.01810 | 0.05524 | 0.1655 |
| Lognormal, $\sigma_{\ln} = 0.45$ | 0.01915 | 0.05221 | 0.1564 |
| Lognormal, $\sigma_{\ln} = 0.80$ | 0.02240 | 0.04464 | 0.1337 |
| Mixture *A* | 0.02178 | 0.04592 | 0.1376 |
| Mixture *B* | 0.02142 | 0.04669 | 0.1399 |

All five distributions satisfy this conditional test at $f_{\rm PBH} = 10^{-3}$ and throughout the abundance scan up to $3 \times 10^{-3}$, where the largest $\mathcal{I}$ is 0.166. The expected PBH count is $N_{\rm exp}^{\rm PBH} = -\ln(0.05)\mathcal{I}$. The omitted mass fraction outside the tabulated range is below $5.2 \times 10^{-11}$ for these distributions; changing to log-linear interpolation changes $J$ by less than 0.025%. Figure 9 displays the contributions across mass. This calculation tests one specified survey response. Accretion constraints from the cosmic microwave background [35] and merger-population data provide complementary information with their own physical and statistical assumptions.

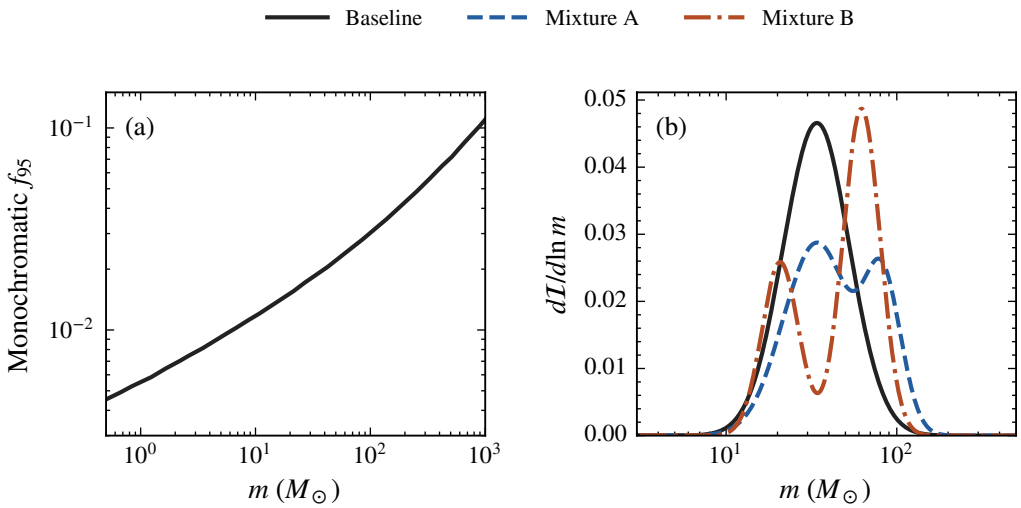



**Figure 9.** Conditional abundance calculation using the authors' OGLE table. (**a**) Strict monochromatic 95% upper limit under the zero-PBH-lens assumption. (**b**) Contribution per logarithmic mass interval, $d\mathcal{I}/d\ln m = f_{\rm PBH} m^2 p(m)/[\langle m \rangle f_{\max}(m)]$, for the baseline lognormal and the two mixtures, at $f_{\rm PBH} = 10^{-3}$. Integrating panel (**b**) over $d\ln m$ gives the normalized expected counts in Table 4; the calculation uses the full tabulated range.

### *5.3. Interpretation and Scope*

The crossed comparison separates the population prescription from coalescence emission; the time-only control further separates redshift weighting from mass selection. Refitting then measures how closely simpler templates reproduce these calculated spectra. The phenomenological control is a comparison template, not a stellar-origin formation model, so its residuals do not establish primordial-versus-stellar discrimination.

Complementary population data can restrict these degeneracies. Stellar-origin binary histories combine star formation, metallicity, and merger delays [16,36]; SMBHB models connect binary populations to host-galaxy observations [4,37]. GW–galaxy angular cross-correlations add spatial information beyond the isotropic spectrum [38]. These observations constrain population ingredients entering the spectral interpretation.

The physical population calculations use the unclustered, low-abundance early two-body channel. Its analytic suppression model retains an approximate mean-neighbour prescription; distributions spanning widely separated mass scales can require a more detailed environmental treatment [8]. The mixtures tested here have component medians separated by factors of at most three. Perturbed survivors, three-body formation, initial clustering, and accretion-driven mass evolution are distinct physical extensions [12,13]. The general integral admits correlated mass, redshift, and spin distributions, but the present numerical formation benchmark remains separable in mass and time. The waveform comparisons use related Phenom models with selected higher modes and modest equal aligned spins; they leave cross-family waveform systematics, precession, and residual eccentricity for further study.

Equation (13) predicts an ensemble energy density. Its relation to a finite observation depends on source overlap, selection, and subtraction [39]. A statistical population comparison additionally requires detector covariance, other astrophysical contributions, and constraints on formation inputs. Instrument sensitivity calculations, including those for LISA [40], help specify such an analysis, whereas the residuals reported here quantify agreement between theoretical spectra.

## 6. Conclusions

We have evaluated a published early two-body PBH formation prescription with full coalescence emission and compared it with a phenomenological independent-pair population. The mass-dependent rate, conversion from number to mass-fraction density, and early suppression determine the merging distribution. Direct quadrature, limiting cases, and resolution tests check the numerical implementation.

At the fiducial mass and width, replacing hard-ISCO inspiral emission with IMRPhenomD shifts the peak upward by factors of 5.45 and 5.81 for the phenomenological and early-channel populations. With IMR fixed, replacing the phenomenological prescription by the early channel lowers the peak by 16.6% and increases its logarithmic half-maximum width by 32.2%. The ablation attributes the broadening almost entirely to redshift weighting: adding the mass weights to that time-only control shifts the peak by $-7.28\%$ and the width by $-0.017\%$. Related IMR prescriptions, higher modes, aligned spins, and formation-input scans quantify further calibration changes. These effects enter the conversion from a turnover frequency to a mass scale.

The free-parameter comparisons measure spectral differences remaining after mass, width, and amplitude adjustment. On 10–300 Hz, the phenomenological template leaves a baseline logarithmic residual of 0.0657 after refitting. Its residual varies across the width–abundance grid and changes with the fitting band. Within the early channel, free lognormal fits reduce the two mass-mixture residuals to 0.0190 and 0.0765. These reductions show how parameter adjustment can absorb differences found at fixed moments or fixed parameters.

The general weighted-response representation relates the remaining differences to the distribution of source properties contributing to the background.

The five tested initial distributions also satisfy the OGLE abundance check throughout $f_{\rm PBH} = 3 \times 10^{-4}$–$3 \times 10^{-3}$ under the adopted zero-PBH-lens and halo assumptions. Together, the calculations connect a specified formation channel to its spectral shapes and quantify their approximation by a simpler mass distribution.

**Author Contributions:** Conceptualization, Y.B. and X.Y.; methodology, software, validation, and formal analysis, Y.B.; writing—original draft preparation, Y.B.; writing—review and editing, Y.B. and X.Y.; supervision, X.Y. All authors have read and agreed to the published version of the manuscript.

**Funding:** This research received no external funding.

**Data Availability Statement:** The results reported in this article are synthetic calculations with inputs specified in the text. The calculation and validation code, numerical results, and figure-generation scripts are archived in Zenodo at https://doi.org/10.5281/zenodo.24183488. The archive files are under embargo until 13 December 2026 and will be publicly accessible from that date. The public OGLE upper-limit table used in the abundance calculation is available from the source cited in Ref. [34]. Published LVK summary values used for observational context are cited in Section 5.1.

**Acknowledgments:** Y.B. thanks X.Y. for guidance. We thank the anonymous reviewers for their constructive comments, which helped improve the clarity and scope of this work.

**Conflicts of Interest:** The authors declare no conflicts of interest.

## Appendix A. Reproducibility and Numerical Diagnostics

The calculations use Python 3.11.8, NumPy 1.26.4, SciPy 1.13.1, mpmath 1.3.0, and LALSuite 7.26.16 (LAL 7.7.1 and LALSimulation 6.2.1); the figures are generated with Matplotlib 3.10.0 and SciencePlots 2.2.2. PhenomD is called without tides, at a reference total mass of $60M_\odot$, and tabulated at 4097 logarithmic frequencies $10^{-8} \leq u \leq 0.2$ per mass-ratio node. XAS/XHM use the same number of samples up to $u = 0.3$. Mass scaling supplies other total masses. Below the table, we use the Newtonian limit, checked for PhenomD at $u = 10^{-9}$ to within $6 \times 10^{-6}$ for $q = 1, 1/4, 1/18$. The mass integral extends to eight standard deviations in $x$; cosmic age includes radiation. Local cubic interpolation in $\ln f$ locates the peak, and shape-preserving interpolation with bracketed roots locates the half-maximum crossings.

Independent Gauss–Hermite integration with 120 nodes in each initial log mass gives the full local rate 2.9305244 $\mathrm{Gpc}^{-3}\,\mathrm{yr}^{-1}$, agreeing with production to better than $10^{-12}$ fractionally. At $\sigma_{\ln} = 0.01$, the rate differs from the monochromatic limit by $6.2 \times 10^{-5}$. Direct torque-suppression quadrature, with a special-function check against arbitrary precision, is also propagated through the PhenomD background at $\sigma_{\ln} = 0.2, 0.45, 0.8$: local rates change by at most 0.404%, peaks by 0.038%, and absolute spectra by 0.554% over 10–300 Hz relative to the published approximation. Its 161-point logarithmic suppression table spans $0.001 \leq M_{\rm tot}/\langle m \rangle \leq 500$; off-grid checks against fresh quadrature differ by less than $6 \times 10^{-6}$. At the two extreme ratios $f_{\rm PBH}/\sigma_M$ in Figure 5, propagating the direct suppression integral changes the normalized XHM shape by at most 0.111% in the same band and the local rate by at most 1.022%.

For the mass mixtures, the direct suppression integral is evaluated in the number-weighted convention of Ref. [11]:

$$S_E = \frac{e^{-\bar{N}}}{\Gamma(21/37)} \int_0^\infty dv\, v^{-16/37} \exp\left[ -\bar{N} \left\langle F\left( \frac{mv}{\langle m \rangle \bar{N}} \right) \right\rangle_p - \frac{3\sigma_M^2 v^2}{10 f_{\rm PBH}^2} \right], \tag{A1}$$

where $F(x) = {}_1F_2(-1/2; 3/4, 5/4; -9x^2/16) - 1$ and $\langle F \rangle_p = \int p(m) F \, dm$. For a mixture, this expectation includes each component with its number fraction. We integrate the joint log-mass density in $x = \ln[\sqrt{m_1 m_2}/(30M_\odot)]$ and $y = \ln(m_1/m_2)/2 \geq 0$, including the Jacobian and symmetry factor $4m_1m_2$. For the baseline single lognormal, this implementation reproduces the earlier integrator to $7 \times 10^{-15}$ fractionally with identical suppression. Halving the logarithmic spacing, doubling the mass-ratio nodes, and refining the suppression expectation and table changes the five new spectra by less than 0.0035% over 10–300 Hz. Peak and width changes are below 0.0005%. Direct suppression changes their spectra by at most 0.68% relative to the moment-based interpolation; Table 2 consistently uses the direct result. The supplied script and tables give all mixture weights and quadrature settings.

The XHM mode sum agrees with angular integration of the two polarizations to better than $4.2 \times 10^{-7}$ for $q = 1, 1/4$, at six frequencies from 10 to 600 Hz and $M_{\rm tot} = 60M_\odot$, using eight inclination-cosine Gauss nodes and eight orbital phases. Refinement to 8193 response samples, 96 mass-ratio nodes, a logarithmic step of 0.0025, and 1201 output frequencies changes spectra by at most 0.080% for XAS at $\sigma_{\ln} = 0.2$ and 0.016% for XHM at $\sigma_{\ln} = 0.45, 0.8$, including the two broad-distribution spin tests; peak and width changes are below 0.0003%. A separate direct population integral uses 80 Gauss–Hermite nodes in $x$, 48 Gauss–Legendre nodes in $|y|$, and 240 in $\ln(1+z)$, with waveform calls at the actual source frequencies. It agrees with production to within $7.91 \times 10^{-5}$ fractionally at 10, 25, 100, and 300 Hz, without using convolution or a response table.

The two-summary match solves a bracketed width root, uses mass similarity, and then recomputes the spectrum at the matched parameters. The full-spectrum fits profile out $\ln A$ as the mean of $\ln \Omega_{\rm tgt} - \ln \Omega_{\rm tmp}$ and optimize mass and width within the stated bounds. A cubic template grid initializes a bounded multi-start search; each reported solution is then refined with directly recomputed population integrals. The grid contains 39 initial widths and 1001 frequencies; its profiled shape differs from the direct result by at most 0.0004% at the main fitted points. Refining the mass/redshift spacing, mass-ratio quadrature, and suppression integral for both target and template changes the logarithmic residual by less than $5 \times 10^{-6}$ in the six mixture fits and three broad, high-abundance fits. The separate short-band bound check extends the template grid to 59 widths.

For the three main 10–300 Hz fits (the baseline early-channel target and mixtures $A, B$), we extend both target and template to $q \geq 10^{-3}$, holding the saved fitted masses and widths fixed and refitting only amplitude. The logarithmic residual changes by $-4.83 \times 10^{-5}$, $+3.74 \times 10^{-5}$, and $+3.21 \times 10^{-5}$, respectively. This checks sensitivity at the reported solutions using the waveform extrapolation described in Section 2.3.

Independent 512-node Gauss–Hermite integration in the initial number measure, including the factor $m/\langle m \rangle$, reproduces the abundance integrals to within $2.5 \times 10^{-6}$ fractionally. Assigning the omitted mass tails the largest tabulated response $1/f_{\rm max}$ changes $J$ by less than $4.2 \times 10^{-10}$ fractionally for the five target distributions. This is a tail-sensitivity test using an assigned response outside the survey table.

The source package supplies the fit points, boundary flags, numerical checks, and calculation and plotting scripts with reproduction instructions.

## References

1. Agazie, G. et al. [The NANOGrav Collaboration] The NANOGrav 15 yr Data Set: Evidence for a Gravitational-wave Background. *Astrophys. J. Lett.* **2023**, *951*, L8. https://doi.org/10.3847/2041-8213/acdac6.
2. Hellings, R.W.; Downs, G.S. Upper limits on the isotropic gravitational radiation background from pulsar timing analysis. *Astrophys. J. Lett.* **1983**, *265*, L39–L42. https://doi.org/10.1086/183954.
3. Antoniadis, J. et al. [EPTA Collaboration and InPTA Collaboration] The second data release from the European Pulsar Timing Array: III. Search for gravitational wave signals. *Astron. Astrophys.* **2023**, *678*, A50. https://doi.org/10.1051/0004-6361/202346844.

4. Agazie, G. et al. [The NANOGrav Collaboration] The NANOGrav 15 yr Data Set: Constraints on Supermassive Black Hole Binaries from the Gravitational-wave Background. *Astrophys. J. Lett.* **2023**, *952*, L37. https://doi.org/10.3847/2041-8213/ace18b. Erratum in *Astrophys. J. Lett.* **2026**, *1006*, L67. https://doi.org/10.3847/2041-8213/ae8764.
5. Green, A.M.; Kavanagh, B.J. Primordial black holes as a dark matter candidate. *J. Phys. G Nucl. Part. Phys.* **2021**, *48*, 043001. https://doi.org/10.1088/1361-6471/abc534.
6. Carr, B.; Kohri, K.; Sendouda, Y.; Yokoyama, J. Constraints on primordial black holes. *Rep. Prog. Phys.* **2021**, *84*, 116902. https://doi.org/10.1088/1361-6633/ac1e31.
7. Sasaki, M.; Suyama, T.; Tanaka, T.; Yokoyama, S. Primordial black holes—perspectives in gravitational wave astronomy. *Class. Quantum Grav.* **2018**, *35*, 063001. https://doi.org/10.1088/1361-6382/aaa7b4.
8. Raidal, M.; Vaskonen, V.; Veermäe, H. Formation of primordial black hole binaries and their merger rates. *arXiv* **2024**, arXiv:2404.08416.
9. Sasaki, M.; Suyama, T.; Tanaka, T.; Yokoyama, S. Primordial Black Hole Scenario for the Gravitational-Wave Event GW150914. *Phys. Rev. Lett.* **2016**, *117*, 061101. https://doi.org/10.1103/PhysRevLett.117.061101. Erratum in *Phys. Rev. Lett.* **2018**, *121*, 059901. https://doi.org/10.1103/PhysRevLett.121.059901.
10. Ali-Haïmoud, Y.; Kovetz, E.D.; Kamionkowski, M. Merger rate of primordial black-hole binaries. *Phys. Rev. D* **2017**, *96*, 123523. https://doi.org/10.1103/PhysRevD.96.123523.
11. Raidal, M.; Spethmann, C.; Vaskonen, V.; Veermäe, H. Formation and evolution of primordial black hole binaries in the early universe. *J. Cosmol. Astropart. Phys.* **2019**, *2019*, 018. https://doi.org/10.1088/1475-7516/2019/02/018.
12. Vaskonen, V.; Veermäe, H. Lower bound on the primordial black hole merger rate. *Phys. Rev. D* **2020**, *101*, 043015. https://doi.org/10.1103/PhysRevD.101.043015.
13. Franciolini, G.; Kritos, K.; Berti, E.; Silk, J. Primordial black hole mergers from three-body interactions. *Phys. Rev. D* **2022**, *106*, 083529. https://doi.org/10.1103/PhysRevD.106.083529.
14. Depta, P.F.; Schmidt-Hoberg, K.; Schwaller, P.; Tasillo, C. Signals of merging supermassive primordial black holes in pulsar timing arrays. *Phys. Rev. Res.* **2025**, *7*, 013196. https://doi.org/10.1103/PhysRevResearch.7.013196.
15. Abbott, B. P. et al. [LIGO Scientific Collaboration and Virgo Collaboration] GW150914: Implications for the Stochastic Gravitational-Wave Background from Binary Black Holes. *Phys. Rev. Lett.* **2016**, *116*, 131102. https://doi.org/10.1103/PhysRevLett.116.131102.
16. Mukherjee, S.; Silk, J. Can we distinguish astrophysical from primordial black holes via the stochastic gravitational wave background? *Mon. Not. R. Astron. Soc.* **2021**, *506*, 3977–3985. https://doi.org/10.1093/mnras/stab1932.
17. Ebersold, M.; Regimbau, T. Uncertainty in predicting the stochastic gravitational wave background from compact binary coalescences. *Phys. Rev. D* **2026**, *113*, 044026. https://doi.org/10.1103/p3dn-x5sp.
18. Ajith, P.; Babak, S.; Chen, Y.; Hewitson, M.; Krishnan, B.; Whelan, J.T.; Brügmann, B.; Diener, P.; Gonzalez, J.; Hannam, M.; et al. A phenomenological template family for black-hole coalescence waveforms. *Class. Quantum Grav.* **2007**, *24*, S689–S699. https://doi.org/10.1088/0264-9381/24/19/S31.
19. Khan, S.; Husa, S.; Hannam, M.; Ohme, F.; Pürrer, M.; Jiménez Forteza, X.; Bohé, A. Frequency-domain gravitational waves from non-precessing black-hole binaries. II. A phenomenological model for the advanced detector era. *Phys. Rev. D* **2016**, *93*, 044007. https://doi.org/10.1103/PhysRevD.93.044007.
20. Pratten, G.; Husa, S.; García-Quirós, C.; Colleoni, M.; Ramos-Buades, A.; Estellés, H.; Jaume, R. Setting the cornerstone for the IMRPhenomX family of models for gravitational waves from compact binaries: The dominant harmonic for non-precessing quasi-circular black holes. *Phys. Rev. D* **2020**, *102*, 064001. https://doi.org/10.1103/PhysRevD.102.064001.
21. García-Quirós, C.; Colleoni, M.; Husa, S.; Estellés, H.; Pratten, G.; Ramos-Buades, A.; Mateu-Lucena, M.; Jaume, R. IMRPhenomXHM: A multi-mode frequency-domain model for the gravitational wave signal from non-precessing black-hole binaries. *Phys. Rev. D* **2020**, *102*, 064002. https://doi.org/10.1103/PhysRevD.102.064002.
22. Peters, P.C. Gravitational Radiation and the Motion of Two Point Masses. *Phys. Rev.* **1964**, *136*, B1224–B1232. https://doi.org/10.1103/PhysRev.136.B1224.
23. Peters, P.C.; Mathews, J. Gravitational Radiation from Point Masses in a Keplerian Orbit. *Phys. Rev.* **1963**, *131*, 435–440. https://doi.org/10.1103/PhysRev.131.435.
24. Phinney, E.S. A Practical Theorem on Gravitational Wave Backgrounds. *arXiv* **2001**, arXiv:astro-ph/0108028.
25. Aghanim, N. et al. [Planck Collaboration] Planck 2018 results. VI. Cosmological parameters. *Astron. Astrophys.* **2020**, *641*, A6. https://doi.org/10.1051/0004-6361/201833910. Corrigendum in *Astron. Astrophys.* **2021**, *652*, C4. https://doi.org/10.1051/0004-6361/201833910e.
26. Abbott, R. et al. [LIGO Scientific Collaboration, Virgo Collaboration, and KAGRA Collaboration] Upper limits on the isotropic gravitational-wave background from Advanced LIGO and Advanced Virgo's third observing run. *Phys. Rev. D* **2021**, *104*, 022004. https://doi.org/10.1103/PhysRevD.104.022004.

27. Abac, A.G. et al. [The LIGO Scientific Collaboration, the Virgo Collaboration, the KAGRA Collaboration] Upper Limits on the Isotropic Gravitational-Wave Background from the first part of LIGO, Virgo, and KAGRA's fourth Observing Run. *arXiv* **2025**, arXiv:2508.20721.
28. Abac, A.G. et al. [The LIGO Scientific Collaboration, the Virgo Collaboration, the KAGRA Collaboration] Updated Upper Limits on the Isotropic Gravitational-Wave Background from LIGO, Virgo, and KAGRA Data through April 2025. *arXiv* **2026**, arXiv:2608.23477.
29. Allen, B.; Romano, J.D. Detecting a stochastic background of gravitational radiation: Signal processing strategies and sensitivities. *Phys. Rev. D* **1999**, *59*, 102001. https://doi.org/10.1103/PhysRevD.59.102001.
30. Romano, J.D.; Cornish, N.J. Detection methods for stochastic gravitational-wave backgrounds: A unified treatment. *Living Rev. Relativ.* **2017**, *20*, 2. https://doi.org/10.1007/s41114-017-0004-1.
31. LIGO Scientific Collaboration; Virgo Collaboration; KAGRA Collaboration. GWTC-4.0: Population Properties of Merging Compact Binaries. *arXiv* **2025**, arXiv:2508.18083.
32. Carr, B.; Raidal, M.; Tenkanen, T.; Vaskonen, V.; Veermäe, H. Primordial black hole constraints for extended mass functions. *Phys. Rev. D* **2017**, *96*, 023514. https://doi.org/10.1103/PhysRevD.96.023514.
33. Mróz, P.; Udalski, A.; Szymański, M.K.; Soszyński, I.; Wyrzykowski, Ł.; Pietrukowicz, P.; Kozłowski, S.; Poleski, R.; Skowron, J.; Skowron, D.; et al. No massive black holes in the Milky Way halo. *Nature* **2024**, *632*, 749–751. https://doi.org/10.1038/s41586-024-07704-6.
34. Mróz, P.; Udalski, A.; Szymański, M.K.; Soszyński, I.; Wyrzykowski, Ł.; Pietrukowicz, P.; Kozłowski, S.; Poleski, R.; Skowron, J.; Skowron, D.; et al. OGLE Data for No Massive Black Holes in the Milky Way Halo. Numerical 95% Upper-Limit Table. 2024. Available online: https://www.astrouw.edu.pl/ogle/ogle4/LMC_OPTICAL_DEPTH/OGLE_PBH_limits.txt (accessed on 3 November 2026).
35. Ali-Haïmoud, Y.; Kamionkowski, M. Cosmic microwave background limits on accreting primordial black holes. *Phys. Rev. D* **2017**, *95*, 043534. https://doi.org/10.1103/PhysRevD.95.043534.
36. Madau, P.; Dickinson, M. Cosmic Star-Formation History. *Annu. Rev. Astron. Astrophys.* **2014**, *52*, 415–486. https://doi.org/10.1146/annurev-astro-081811-125615.
37. Kormendy, J.; Ho, L.C. Coevolution (Or Not) of Supermassive Black Holes and Host Galaxies. *Annu. Rev. Astron. Astrophys.* **2013**, *51*, 511–653. https://doi.org/10.1146/annurev-astro-082708-101811.
38. Yang, K.Z.; Mandic, V.; Scarlata, C.; Banagiri, S. Searching for cross-correlation between stochastic gravitational-wave background and galaxy number counts. *Mon. Not. R. Astron. Soc.* **2021**, *500*, 1666–1672. https://doi.org/10.1093/mnras/staa3159.
39. Rosado, P.A. Gravitational wave background from binary systems. *Phys. Rev. D* **2011**, *84*, 084004. https://doi.org/10.1103/PhysRevD.84.084004.
40. Robson, T.; Cornish, N.J.; Liu, C. The construction and use of LISA sensitivity curves. *Class. Quantum Grav.* **2019**, *36*, 105011. https://doi.org/10.1088/1361-6382/ab1101.


**Disclaimer/Publisher's Note:** The statements, opinions and data contained in all publications are solely those of the individual author(s) and contributor(s) and not of MDPI and/or the editor(s). MDPI and/or the editor(s) disclaim responsibility for any injury to people or property resulting from any ideas, methods, instructions or products referred to in the content.